Systems/Circuits

Behavioral State-Dependent Modulation of Prefrontal Cortex Activity by Respiration

Shani Folschweiller[1,2] and Jonas-Frederic Sauer[1]

[1]Institute of Physiology 1, Medical Faculty, University of Freiburg, D-79104 Freiburg, Germany and [2]Faculty of Biology, University of Freiburg, D-79104 Freiburg, Germany

Respiration-rhythmic oscillations in the local field potential emerge in the mPFC, a cortical region with a key role in the regulation of cognitive and emotional behavior. Respiration-driven rhythms coordinate local activity by entraining fast γ oscillations as well as single-unit discharges. To what extent respiration entrainment differently engages the mPFC network in a behavioral state-dependent manner, however, is not known. Here, we compared the respiration entrainment of mouse PFC local field potential and spiking activity (23 male and 2 female mice) across distinct behavioral states: during awake immobility in the home cage (HC), during passive coping in response to inescapable stress under tail suspension (TS), and during reward consumption (Rew). Respiration-driven rhythms emerged during all three states. However, prefrontal γ oscillations were more strongly entrained by respiration during HC than TS or Rew. Moreover, neuronal spikes of putative pyramidal cells and putative interneurons showed significant respiration phase-coupling throughout behaviors with characteristic phase preferences depending on the behavioral state. Finally, while phase-coupling dominated in deep layers in HC and Rew conditions, TS resulted in the recruitment of superficial layer neurons to respiration. These results jointly suggest that respiration dynamically entrains prefrontal neuronal activity depending on the behavioral state.

Key words: emotional behavior; prefrontal cortex; respiration; respiration-related rhythm

---

Significance Statement

The mPFC, through its extensive connections (e.g., to the amygdala, the striatum, serotoninergic and dopaminergic nuclei), flexibly regulates cognitive behaviors. Impairment of prefrontal functions can lead to disease states, such as depression, addiction, or anxiety disorders. Deciphering the complex regulation of PFC activity during defined behavioral states is thus an essential challenge. Here, we investigated the role of a prefrontal slow oscillation that has recently attracted rising interest, the respiration rhythm, in modulating prefrontal neurons during distinct behavioral states. We show that prefrontal neuronal activity is differently entrained by the respiration rhythm in a cell type- and behavior-dependent manner. These results provide first insight into the complex modulation of prefrontal activity patterns by rhythmic breathing.

Introduction

Rhythmic breathing influences cognitive functions, including emotional discrimination as well as perception and memory in humans (Zelano et al., 2016; Arshamian et al., 2018; Nakamura et al., 2018; Kluger et al., 2021; Grund et al., 2022; Johannknecht and Kayser, 2022) and the expression of fear-related freezing in rodents (Moberly et al., 2018; Bagur et al., 2021). The breathing rhythm is broadcast to cortical circuits via at least two pathways: A well-established re-afferent route emerging from nasal air

flow, and an efference copy signal from the brainstem (Karalis and Sirota, 2022). Air flow in the nasal cavity mechanically activates olfactory sensory neurons in the olfactory epithelium (OE) (Grosmaitre et al., 2007; Connelly et al., 2015), which induce respiration-driven rhythms (RRs) in the local field potential (LFP) of the olfactory bulb (OB) (Adrian, 1942; Courtiol et al., 2011). In mammals, the widespread projections from the OB are well conserved (Lane et al., 2020), and outgoing projections from the OB give rise to broadly distributed RR across cortical and subcortical brain areas (Ito et al., 2014; Yanovsky et al., 2014; Lockmann et al., 2016; Nguyen Chi et al., 2016; Biskamp et al., 2017; Liu et al., 2017; Zhong et al., 2017; Moberly et al., 2018; Tort et al., 2018b; Folschweiller and Sauer, 2022; Karalis and Sirota, 2022). The mPFC as a central control instance of cognitive and emotional behavior displays prominent RR that entrains both ~80 Hz γ oscillations as well as single-unit activity (Biskamp et al., 2017; Liu et al., 2017; Zhong et al., 2017; Karalis and Sirota, 2022; González et al., 2023).

Respiration frequency depends on the behavioral state of the animal. During immobility, mice breathe regularly at ~2-5 Hz, while active states are associated with less regular and faster breathing (Tort et al., 2018b). Interestingly, the entrainment of mPFC circuits is particularly efficient for slow breathing frequencies (Biskamp et al., 2017; Zhong et al., 2017; Bagur et al., 2021; Girin et al., 2021; Karalis and Sirota, 2022). Strong entrainment during slow breathing might be favored by the large air volume flowing through the nasal cavity, hence inducing a strong activation of olfactory sensory neurons. In addition, OB-to-mPFC transmission is particularly responsive to slow breathing frequencies (Bagur et al., 2021).

Despite the established strong influence of respiration on mPFC activity during immobility, the number of studies contrasting defined behavioral states of immobility is limited. Several reports investigated RR during spontaneous immobility (i.e., quiet wakefulness), a behavioral state arguably perceived as "neutral" (Zhong et al., 2017; Tort et al., 2018b; Girin et al., 2021; Mofleh and Kocsis, 2021; Karalis and Sirota, 2022). Other studies investigated RR during "negative emotional states," such as fear conditioning-induced freezing (Moberly et al., 2018; Carney, 2019; Bagur et al., 2021; Karalis and Sirota, 2022), or adverse stimulation during tail suspension (TS) (Biskamp et al., 2017). Finally, slow oscillations in the δ/theta frequency range (~4-10 Hz) show large intertrial phase consistency during reward consumption (Horst and Laubach, 2013; Amarante et al., 2017), in particular for highly rewarding stimuli (Amarante and Laubach, 2021), but the potential roles of RR in organizing prefrontal activity patterns during such immobile states associated with positive experience have so far not been directly investigated. If efficient respiration pacing of neuronal circuits merely depends on the immobile state and the resulting slow breathing rhythm, it would follow that similar patterns of network entrainment should be observed under distinct conditions of awake immobility. As an alternative hypothesis, respiration might contribute differently to information processing during distinct immobility states. Here, we tested these hypotheses in awake mice. Focusing on the mPFC, we probed respiration entrainment during home cage (HC) immobility, stress-related passive coping in the TS, and reward consumption. We find that the entrainment of local network oscillations and neuronal spikes are modulated by respiration in a behavior-dependent manner.

Materials and Methods

Mice. Male ($n = 23$ mice) and female ($n = 2$ mice) C57/Bl6, Ai32 (RCL-ChR2(H134R)/EYFP) (AI32 for short) expressing a channelrhodopsin-2 (ChR2)-EYFP fusion protein with an upstream STOP cassette flanked by loxP sites, and Ai32 crossed with mice expressing Cre-recombinase under the control of the parvalbumin promoter (The Jackson Laboratory, strains #012569 and #008069), 7-23 weeks old at the day of electrode implantation, were used in this study. In the latter mouse line, ChR-2 is expressed specifically in parvalbumin-containing interneurons. Mice were housed under 12 h light/dark cycle (light on at 7:00 A.M., group-housing with 2-4 mice per cage, single-housing after implantation of tetrode/silicon probe microdrives). All experiments were conducted during the light phase. While the low number of females in our dataset did not allow us to address potential sex differences, results from females were consistent with those originating from males. All experiments were performed in agreement with national legislation and were approved by the Regierungspräsidium Freiburg (license numbers L19-01, G18-69, G18-145, G21-76).

Electrode implantation and recording. Under general anesthesia (isoflurane: induction: 3%, maintenance: 1%-2%), the skull was exposed

from the tip of the nose to the cerebellum. An ~0.8 mm hole, placed ~1 mm lateral to the midline, was drilled in the rostral part of the nasal bone to insert a silver wire de-insulated ~0.5 mm from the tip between the bone and the OE. In 3 mice, a second hole was drilled on the other side to insert a thermocouple (TC, 80 μm diameter, Omega Engineering, part 5TC-TT-KI-40-1 M) into the nasal cavity. The OE was protected using Vaseline and wires cemented (Super-Bond Universal polymer and Quick monomer) in place. Two grounding screws were implanted in the skull ~2 mm around the lambdoid suture, and an additional stabilizing screw in the rostro-medial part of the parietal bone. Ipsilateral to the OE LFP wire, a hole was drilled above the mPFC and a silicon probe (Cambridge Neurotech, ASSY-156P, four shanks) coated with DiD (Vybrant, Invitrogen) or custom-made tetrodes (California Fine Wire, Tungsten 99.95% CS) mounted on a microdrive were implanted at AP 1.9, ML 0.1/0.5, DV −1.0/−1.7. We found no difference in spike waveform properties or single-unit firing rates between tetrode and silicon probe recordings (data not shown). Mice were single-housed after the implantation. Postsurgical pain was relieved using carprofen and buprenorphine subcutaneously and in the drinking water, and mice were allowed to recover for at least 3 d. On recording days, the headstage (Intan Technologies, RHD2132/RHD2164) was mounted and the electrodes were lowered by 100 μm. Data acquisition commenced at least 10 min after moving the electrodes using GUI software (Open Ephys), at a sampling frequency of 30 kHz, except specified otherwise. Synchronization between videos or laser stimulation and recordings was achieved through Arduino-based circuits or by using the Ethovision software (Noldus).

Behavior. Recordings were performed in a sound-attenuating chamber. HC ($n = 10$ mice, age 12.4 w (SD 1.6 w), 8 males, 2 females, 8 with tetrodes and 2 with silicon probe recording) was acquired in an ~15 min recording session. Then the mouse was subjected to 6 min of TS, during which it usually displayed alternatively struggle and immobility phases. Recording sessions were repeated to a maximum 5 times per mouse with at least a day between recording sessions. For reward consumption (Rew), the mice [$n = 9$, age 18.9 w (SD 7.5 w), 9 males, 7 with tetrodes and 2 with silicon probes] were food-restricted and performed either an olfactory-guided working memory task ($n = 4$ mice) to obtain 20 mg rewards, or a delayed non-match-to-place alternation task in a T-maze with semirandom forced sampling trials ($n = 5$ mice) to obtain 45 mg rewards (Bio-Serv, Dustless Precision Pellets, F0071/F0021). In this study, we only report results of the periods of Rew. Immobility periods were manually selected based on accelerometer readout of the recording amplifier in case of (HC and TS), or using an automated detection on a metric obtained from accelerometer and location (resulting from the tracking option of the Ethovision software, Noldus) relative to the reward delivery location ($n = 8$ mice), or simply location of the mouse in the reward zone (four sessions of 2 mice). Single units from mice ($n = 2$) resulting from the crossing of Ai32 and PV^{cre} were recorded while blue laser pulses (472 nm) were delivered at a power of 5.7 ± 2 mW through a custom-made optic fiber (200 μm diameter, placed ~5 mm above the recording sites).

Histology. After recording, the mice were terminally anesthetized with urethane (10%, 20 μl/g of body mass) or a mix of ketamine (1.6%) and xylazine (0.12%, 6.25 μl/g of body mass). The mice were intracardially perfused with ~20 ml of PBS (0.1 M) followed by 4% PFA. Brains were postfixed in 4% PFA overnight, sliced in coronal sections (100 μm, 50 μm for PV immunohistochemistry), and stained with DAPI (1/1000 dilution, ~10 min incubation time). Electrode locations were determined from image stacks obtained with a laser-scanning microscope (Zeiss) based on stereotaxic coordinates (Franklin and Paxinos, 2007). On 3 AI32-PV^{CRE} mice, a PV immunostaining was performed as described previously (Sauer et al., 2015) using rabbit anti-PV27 primary antibody (Swant, 1:1000) and goat anti-rabbit 568 secondary antibody (1:1000).

Validation of OE LFP signals. Simultaneous measurements of TC and OE LFP signals [$n = 3$ male mice, age 10.7 w (SD 0.55 w), sampling frequency: 30 kHz] were performed sequentially during immobility phases in HC, during consumption of randomly presented rewards in the same environment, and during TS. Power spectral density (PSD) was computed with scipy.welch, coherence using the function scipy.

coherence (windows of 1 s, zero-padded to 5 s, data downsampled to 1 kHz). The time lag of maximal cross-correlation between TC and OE LFP signals was obtained from 1-10 Hz bandpass-filtered data.

Characterization of respiration patterns. To characterize the breathing pattern during immobility, only epochs of at least 1 s in duration were used. The OE LFP traces were downsampled to 1 kHz and bandpass-filtered between 1 and 12 Hz for detecting the LFP troughs identified using the maxima π (using the scipy.signal "find_peaks" function selecting peaks >3.1) in the instantaneous phase from the Hilbert transform of the LFP traces. The mean and SD of trough-to-trough durations were then calculated. To detect sniffing bouts, we used a sliding window of 1 s over the OE LFP and computed the spectrogram for each 1 s snippet. To compensate for the short duration of the windows, we used three slepian tapers for a half bandwidth of 1 Hz and averaged the resulting spectrogram. Then, we identified the peak frequency occurring <15 Hz for each window and classified it as sniffing if it was >7 Hz (Wachowiak, 2011; Rojas-Líbano et al., 2018).

PSD, coherence, and directed coherence. To analyze coherence, PSD of the mPFC, directed coherence and modulation of γ oscillation by respiration, a random channel was selected for further analysis. OE and mPFC LFP traces were z-scored using the corresponding function from scipy.stats.mstats; then epochs of immobility were extracted while excluding manually selected artifacts and kept for further analysis only if the total amount of immobility was >30 s. Next, the coherence or PSD over a 2 s Hanning sliding window with an overlap of 0.5 s was computed and averaged using the scipy.signal "coherence" or "welch" function. Directed coherence in the frequency domain was computed in Octave using the function sp2a2_R2 of the NeuroSpec 2.1 toolbox.

Modulation of γ oscillations. After downsampling to 1 kHz, we iterated over γ (from 20 to 150 Hz, steps of 5 Hz, bandpass of 10 Hz) and respiration frequency (from 1 to 13 Hz, steps of 1 Hz, bandpass of 1 Hz). For each pair of frequencies, the mean of the γ envelope (absolute value of the Hilbert transform) as a function of the respiration phase separated in 18 bins was calculated on 4 s nonoverlapping sliding windows. After averaging all windows, the binned γ envelope was converted to probabilities by dividing by the sum. The Kullback–Leibler divergence of the γ amplitude was then calculated as follows:

$$KLD = \sum_{b=1}^{18} g_b \cdot ln(frac{g_b}{u_b})$$

where b is the bin number, g_b is the normalized γ amplitude for the corresponding respiration phase bin among the 18 bins, and u_b is the normalized γ amplitude for the corresponding bin in the case of a uniform distribution and thus was defined as 1/18 for all bins. Comparison of normalized γ amplitude (filtered between 85 and 95 Hz) across behavioral states was performed on the maxima of the normalized γ amplitude for each session, with respiration filtered from 2 to 3 Hz for HC and TS, and from 4 to 5 Hz for Rew.

Spike sorting. A common average computed as the mean of 8-10 randomly selected channels was subtracted from all channels. Recording sections containing artifacts were manually identified and removed. Single units were clustered from 0.3 to 6 kHz bandpass-filtered data using MountainSort (Chung et al., 2017). The obtained clusters were first automatically curated based on isolation [threshold of 0.95 ($n = 2$ mice) or 0.9 ($n = 19$ mice)] and noise overlap (0.05) and further manually curated based on clean spike shapes, autocorrelograms with clear refractory periods and a firing rate >0.5 Hz over the entire recording session.

Firing rate. Firing rate was determined as the mean number of spikes occurring per second. The epoch selected for comparison between putative interneurons (pINs) and putative pyramidal cell (pPC) was the entire HC recording, including active and inactive periods. The comparison of firing rate across layers and behavioral states was performed during immobility periods only.

Characterization of functionally relevant pPCs. To determine cells with a significant firing response at transition between immobile and active states, 4 s snippets of the spike train of individual prefrontal units centered on immobility onset or offset were binned (bin size: 40 ms), z-scored, and summed for all occurring period of immobility lasting >1 s. The total sum of the z-scored firing response over the 4 s was then compared with the value obtained by shuffling the bin order (1000 iterations) for each immobility period. If the obtained value for the firing response was higher or lower than the 95th highest or lowest percentile of the shuffled distribution, it was considered as significantly changing its firing response at immobility transitions.

Optogenetic identification of parvalbumin-expressing interneurons (PVIs) and spike shape. To establish light-responsive single units in the recording from the Ai32 $\times$ PV^{CRE} mice [$n = 3$ male mice with tetrode recording, age 9.7 w (SD 0.5 w)], we aimed at identifying fast and reliable spiking responses after laser onset: the spike trains were first convolved with a Gaussian function (SD 0.25 ms) using the "fftconvolve" function of scipy.signal. We then summed up the snippets of the convolved spike train of the single unit of interest occurring in the 50 ms before and 50 ms after laser onsets. If the first peak maximum of activity after laser onset was higher than a threshold set as the mean prestimulus activity plus 8 times its SD, the unit was considered as light-responsive. Using different standard deviation thresholds (1, 2, 4, 16) yielded identical results.

To measure the width of spike waveforms, we first bandpass-filtered (0.3-6 kHz) the channel with the largest negative deflection of the unit of interest. Then snippets of recordings centered at the minima of the trough of all detected spikes were average. Spike width was defined as the time from the trough to the following peak. PINs were defined as single units with a spike width <0.45 ms and pPCs as the ones with a spike width >0.53 ms.

Respiration coupling of single units. For the coupling of single units to respiration, the OE LFP was first filtered 1-5 Hz and troughs were identified, as for LFP analysis, as peaks in the Hilbert transform of the filtered signal while additionally preventing the detection of another trough occurring faster than 6 Hz from the previous one. Then, only spikes occurring during the period of immobility of interest were kept for further analysis, and cells with <18 spikes were discarded. Included units had an average of 1363 ± 3021 spikes occurring in the HC condition, 881 ± 1451 spikes in the TS condition, and 1900 ± 3057 for Rew. For each breathing cycle (from trough to trough), the absolute firing rate for each of the 18 respiration phase bins was computed, summed across breathing cycles, and normalized to sum up to one. The same binned firing rate normalized histogram was computed on shuffled spike trains (1000 iterations) by applying the numpy.random "permutation" function to the interspike intervals. If, for any of the respiration phase bins, the normalized firing rate was above the 99th percentile or below the 1st percentile of the shuffled distribution, it was considered as modulated by respiration. For cells with a significant relative increase in the firing rate, the preferred phase was defined as the bin with the highest normalized firing rate.

Experimental design and statistical analysis. Statistics were done with Python 2.7 or 3.9, except for the χ^2 tests, which were performed on http://www.quantpsy.org/chisq/chisq.htm. Statistical tests were performed using the scipy.stats library, except ANOVA (ols function from statsmodels.formula.api), the Dunn *post hoc* test (obtained from github, https://gist.github.com/alimuldal/fbb19b73fa25423f02e8), the Rayleigh test (from pycircstat), and the Two Sample Random Permutation test, which was custom-written as such: A p value was obtained by calculating the probability of the actual circular difference between two angular datasets to be higher than their circular difference after randomly permuting angles between the two group (iterations: 10,000). The Two Sample Random Permutation Test thus outputs a p value but no test statistic. Data are given as mean ± SD, except for boxplots showing the median extending from lower and upper quartiles, whiskers showing extent of the data excluding outliers.

Results

Breathing patterns change with behavioral states

We assessed respiration by recording LFPs from the OE of awake mice (Fig. 1A). Previous studies validated the use of the OE LFP as a means of monitoring respiration in head-
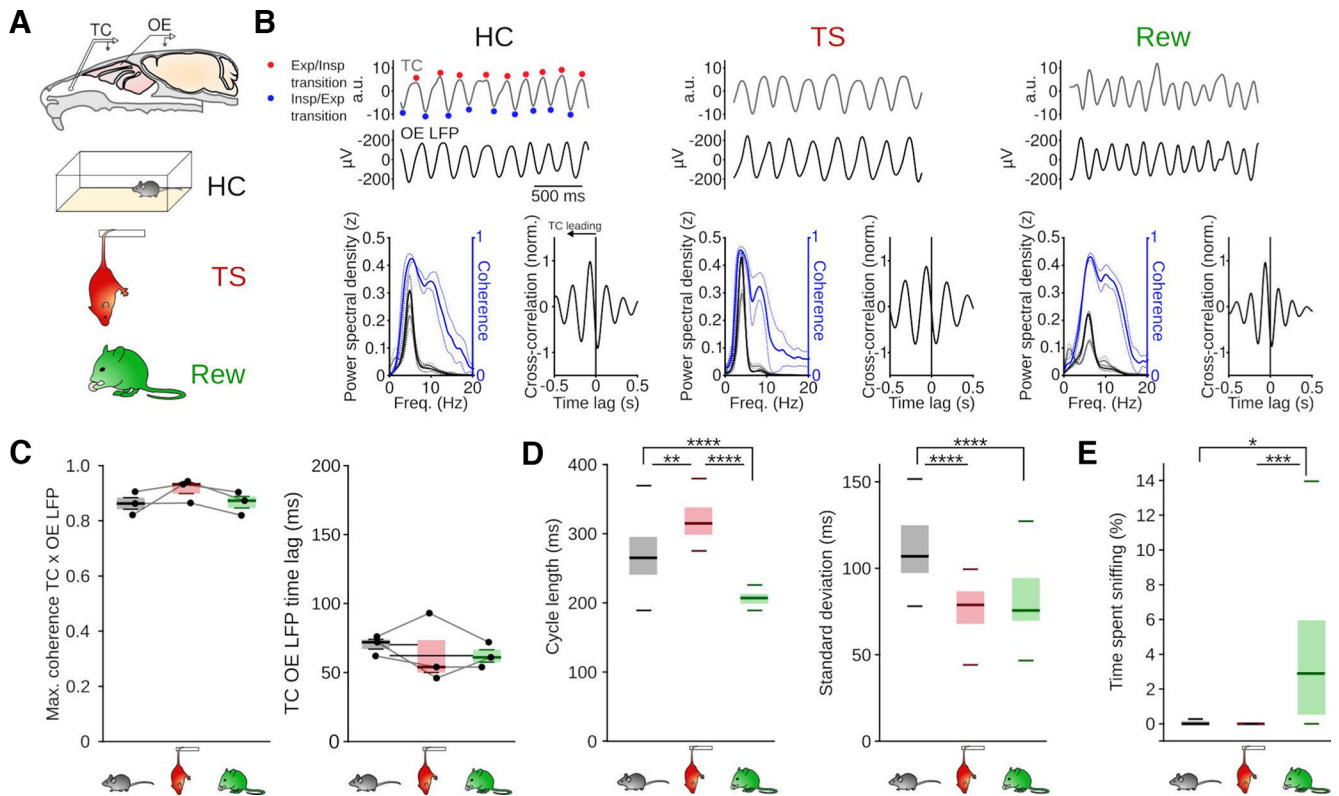
Figure 1. The breathing rhythm as a signature of behavioral states. **A**, Validation of OE LFP recording for monitoring the breathing rhythm. Top, Schematic of simultaneous temperature measurement with a thermocouple (TC) in the nasal cavity and OE LFP recording. Bottom, Schematic of the three behavioral states investigated. **B**, Top, Example traces of TC and OE LFP signals (filtered 1-10 Hz). Bottom left, PSD of TC (gray) and OE LFP signals (black) and TC-OE LFP coherence (blue). Bottom right, Mean cross-correlation between TC and OE LFP signals. Solid lines indicate the mean. Dashed lines indicate SEM ($n = 3$ mice). Exp, Expiration; Insp, Inspiration. **C**, Comparable peak coherence (left, $F = 2.56$, df = 2, $p = 0.192$) and time lag of maximal cross-coherence between TC and OE LFP signals (right, $F = 0.35$, df = 2, $p = 0.722$, $n = 3$ mice, one-way repeated-measures ANOVAs) during the three behavioral states. **D**, Mean duration of a breathing cycle (left, HC vs TS: $z = 3.15$, $p = 4.8 \times 10^{-3}$; HC vs Rew: $z = 4.81$, $p = 4.6 \times 10^{-6}$; TS vs Rew: $z = 8.23$, $p = 5.6 \times 10^{-16}$) and SD of breathing cycle length (right, HC vs TS: $z = 5.29$, $p = 3.7 \times 10^{-7}$; HC vs Rew: $z = 5.20$, $p = 6.16 \times 10^{-7}$; TS vs Rew: $z = 0.43$, $p = 1$) derived from OE LFP measurements during HC, TS, and Rew. HC: $n = 32$ sessions/9 mice; TS: $n = 33$ sessions/10 mice; Rew: $n = 43$ sessions/9 mice. Kruskal–Wallis tests followed by Dunn *post hoc* tests (df = 2). **E**, Quantification of the occurrence of sniffing bouts (HC vs TS: T = 1.04, $p = 0.553$; HC vs Rew: T = −2.92, $p = 0.012$; TS vs Rew: T = −4.14, $p = 0$). HC: $n = 30$ sessions/9 mice; TS: $n = 33$ sessions/10 mice; Rew $n = 43$ sessions/9 mice. One-way ANOVA followed by Tukey tests (df = 1). $*p < 0.05$. $**p < 0.01$. $***p < 0.001$. $****p < 0.0001$.

fixed (Folschweiller and Sauer, 2022) and freely moving mice (Karalis and Sirota, 2022). To confirm the validity of this technique, we simultaneously recorded nasal temperature change with a TC in the nasal cavity as a readout of respiration and OE LFP during immobility phases under HC, TS, and Rew conditions (Fig. 1A–C, for simplicity we refer to the periods of immobility during the three behavioral states as HC, TS, and Rew for the remainder of the text). The two signals showed large coherence with spectral peaks at comparable frequency (Fig. 1B). Moreover, TC and OE LFP signals showed a consistent time lag across behavioral states, confirming that the OE LFP faithfully reflects the breathing rhythm during HC, TS, and Rew (Fig. 1B,C). Consequently, we used the OE LFP as respiration signal for this study, and defined the peak of the oscillation as 0, occurring shortly after onset inspiration, and the trough as transition between π and $-\pi$, occurring shortly after expiration onset (Noto et al., 2018).

We first tested whether the respiratory pattern depended on the behavioral state. During HC, the average length of a breathing cycle was 270 ± 49 ms (i.e., ~ 3.7 Hz) (Fig. 1D), consistent with previous reports of RR oscillations peaking at ~ 3 Hz during immobility (Zhong et al., 2017; Girin et al., 2021; Mofleh and Kocsis, 2021; Karalis and Sirota, 2022). The breathing rhythm was significantly slower during TS, with breathing cycles lasting

318 ± 25 ms (i.e., ~ 3.1 Hz on average) and was significantly faster during Rew with an average 206 ± 11 ms cycle length (i.e., ~ 4.9 Hz) (Fig. 1D). In addition, compared with HC, breathing became highly regular during TS and Rew, as shown by a decreased SD of the cycle duration (Fig. 1D). Finally, the behavioral states were associated with different occurrences of sniffing bouts, which were observed more often during Rew ($5.1 \pm 6.9\%$ of time spent sniffing, $n = 43$ sessions from 9 mice) compared with HC ($1.2 \pm 5\%$, $n = 30$ sessions from 9 mice) and TS ($0.1 \pm 0.2\%$, $n = 33$ sessions from 10 mice, Fig. 1E). Different behavioral states of immobility are thus associated with particular breathing patterns.

Behavioral state-dependent entrainment of prefrontal slow oscillations by respiration

We next asked whether the modulation of prefrontal LFP signals might depend on the behavioral state. To assess neuronal activity alongside respiration, we recorded prefrontal LFP and single-unit activity using tetrodes or silicon probes in freely moving mice (Fig. 2A,B). Consistent with previous reports of RR during quiescence (Zhong et al., 2017; Girin et al., 2021; Mofleh and Kocsis, 2021; Karalis and Sirota, 2022) and TS (Biskamp et al., 2017), we found a peak in the power spectrum of the prefrontal LFP coinciding with the frequency of simultaneously recorded respiration signals during both HC and TS sessions (Fig. 2C,D).
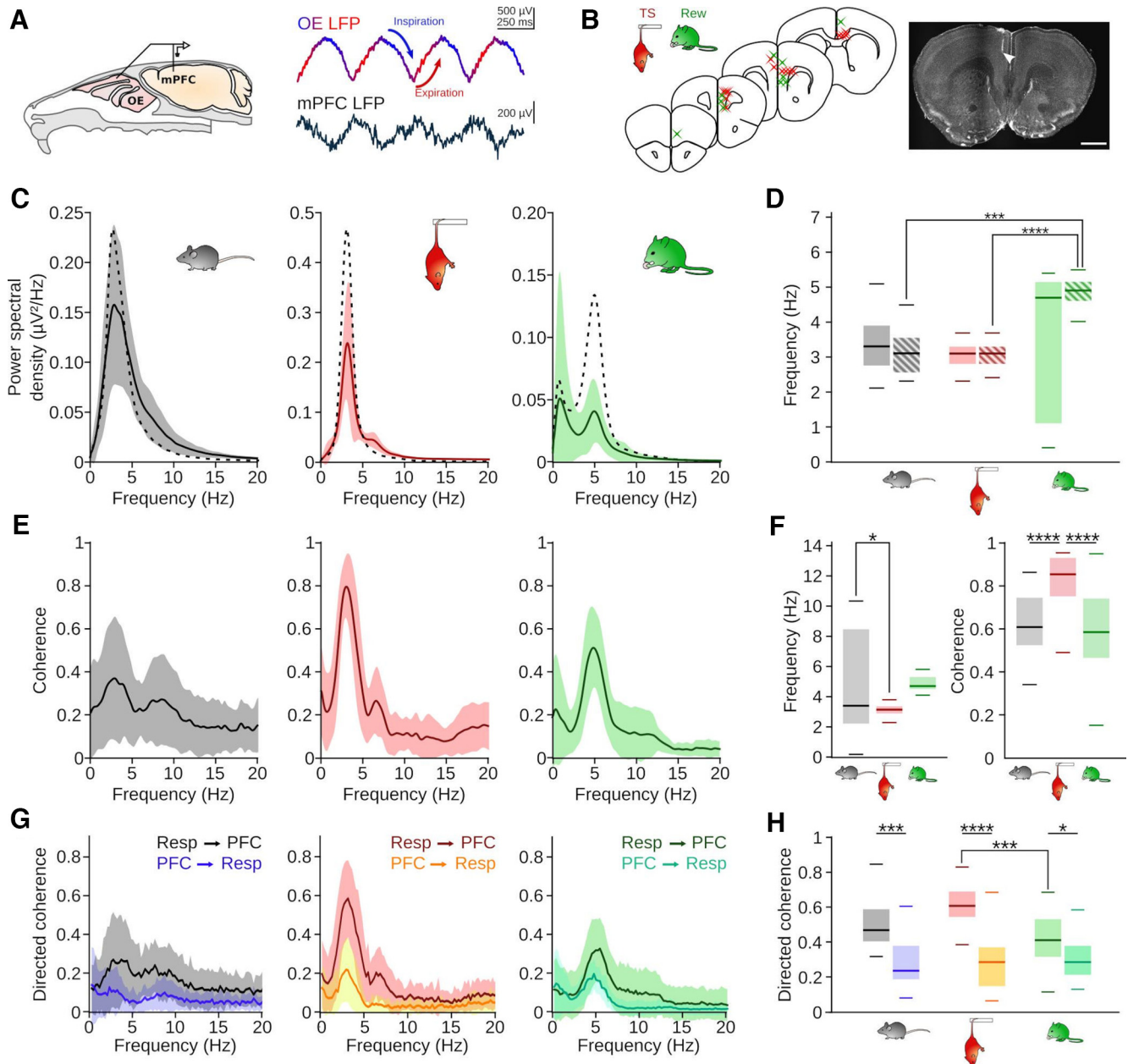
Figure 2. State-dependent emergence of respiration-driven oscillations. ***A***, Left, Schematic of the recording setup. Right, Example traces of the OE and mPFC LFP during TS (1-300 Hz band-pass-filtered). ***B***, Summary (left) and example (right) of recording locations during HC and TS (red) and Rew (green). Scale bar, 1 mm. ***C***, Average (full line indicates mean; shaded area represents SD) PSD of the prefrontal LFP during HC ($n = 27$ sessions/9 mice), TS ($n = 33$ sessions/10 mice), and Rew ($n = 43$ sessions/9 mice). Superimposed dashed line indicates the corresponding mean respiration PSD. ***D***, Frequencies of maximal LFP (full boxes, HC vs TS: $z = 1.37$, $p = 1$; HC vs Rew: $z = 0.91$, $p = 1$; TS vs Rew: $z = 2.51$, $p = 0.109$) and respiration PSD (striped boxes, HC vs TS: $z = 0.01$, $p = 1$; HC vs Rew: $z = 4.16$, $p = 2.8 \times 10^{-4}$; TS vs Rew: $z = 4.43$, $p = 8.5 \times 10^{-5}$). Two-way ANOVA (effect of behavior: $F = 8.01$, df $= 2$, $p = 4.5 \times 10^{-4}$, signal origin: $F = 1.41$, df $= 1$, $p = 0.24$, interaction: $F = 3.27$, df $= 2$, $p = 0.04$) followed by Dunn *post hoc* tests (df $= 5$). ***E***, Coherence between respiration and the mPFC LFP during HC (left, $n = 30$ sessions/8 mice), TS (middle, $n = 31$ sessions 9 mice), and Rew (right, $n = 42$ sessions/9 mice). ***F***, Left, Frequencies of maximal coherence between the respiration and the mPFC LFP (HC vs TS: T $= 2.95$, $p = 0.01$; HC vs Rew: T $= 1.14$, $p = 0.49$; TS vs Rew: T $= -2.03$, $p = 0.11$, one-way ANOVA followed by Tukey *post hoc* tests, df $= 1$). Right, Values of peak coherence shown in ***E*** (HC vs TS: $z = 4.26$, $p = 6.2 \times 10^{-5}$; HC vs Rew: $z = 0.67$, $p = 1$; TS vs Rew: $z = 5.25$, $p = 4.6 \times 10^{-7}$, Kruskal–Wallis test followed by Dunn *post hoc* tests, df $= 2$). ***G***, Directed coherence between respiration and mPFC LFP in forward and reverse direction. ***H***, Maximal directed coherence values of the graphs shown in ***G***. Two-way ANOVA identified effects of behavioral state ($F = 10.03$, df $= 2$, $p = 7 \times 10^{-5}$) and direction ($F = 111.7$, df $= 1$, $p = 5 \times 10^{-21}$) with a state × direction interaction effect ($F = 12.66$, df $= 2$, $p = 6.6 \times 10^{-6}$). Forward vs reverse: HC: $z = 4.31$, $p = 1.5 \times 10^{-4}$; TS: $z = 7.10$, $p = 1.1 \times 10^{-11}$; Rew: $z = 3.08$, $p = 0.019$. Forward: HC vs TS: $z = 2.29$, $p = 0.19$; TS vs Rew: $z = 4.36$, $p = 0.0002$; HC vs Rew: $z = 1.69$, $p = 0.15$; Dunn *post hoc* tests (df $= 5$). *$p < 0.05$. ***$p < 0.001$. ****$p < 0.0001$.

Similarly, Rew was characterized by a spectral RR peak. These slow prefrontal oscillations were coherent with respiration across states (Fig. 2*E*), confirming their RR identity. The peak coherence occurred at lower frequency during TS than HC (Fig. 2*F*), which is consistent with the longer breathing cycle during this state. While we observed prominent RR in the mPFC LFP in all

states, coherence was maximal during TS (Fig. 2*F*). To corroborate that prefrontal RR is driven by nasal respiration, we analyzed directed coherence between respiration and PFC LFP signals (Fig. 2*G*). This analysis revealed larger values in forward (i.e., respiration to mPFC) compared with reverse direction across behaviors. Moreover, consistent with coherence results, directed
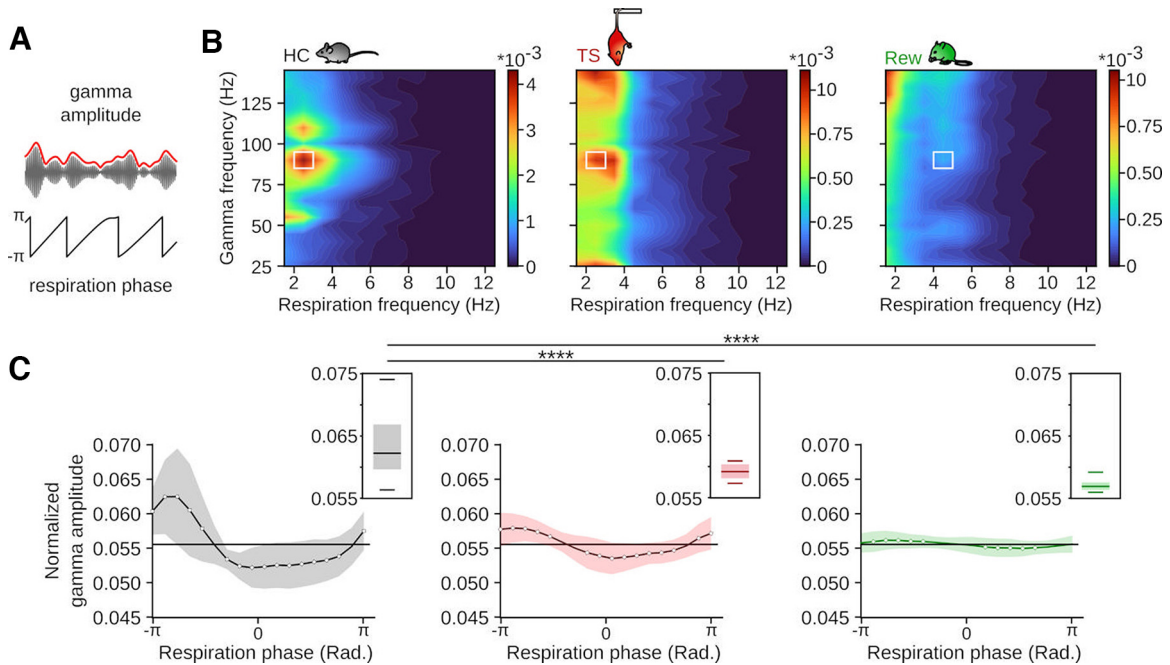
Figure 3. Behavior-specific respiration phase-γ amplitude coupling. **A**, Schematic of the procedure to assess phase-amplitude coupling. Modulation was defined as the Kullback–Leibler divergence of the mean envelope of γ as a function of the phase of the breathing cycle. **B**, Average phase-amplitude modulation during the three behavioral states. Note the different scale applied to TS and Rew. HC: $n = 20$ sessions/8 mice; TS: $n = 28$ sessions/9 mice; Rew: $n = 42$ sessions/9 mice. **C**, Normalized amplitude of the γ envelope (solid line indicates mean; background represents SE, bandpass-filtered 85-95 Hz) as a function of the breathing cycle of the tiles highlighted in white on the corresponding heatmaps in **B**. Boxplot insets, Maximum values of the corresponding normalized respiration-modulated γ amplitude for each recording session (HC vs TS: T = 6.90, $p = 0$, HC vs Rew: T = 9.53, $p = 0$, TS vs Rew: T = 2.34, $p = 0.056$, one-way ANOVA followed by Tukey *post hoc* tests, df = 1). *$p < 0.05$. ****$p < 0.0001$.

coherence was maximal during TS (Fig. 2G,H). Hence, while prefrontal RR occurs during all three conditions of immobility, these oscillations vary with the behavioral state both in strength and frequency.

State-dependent respiration entrainment of γ oscillations
Previous work emphasized that ~80 Hz γ oscillations occur predominantly at the peak/early descending phase of prefrontal RR (Biskamp et al., 2017; Zhong et al., 2017). Consistent with these reports, the amplitude of ~80 Hz γ oscillations was phasemodulated by the respiration signal during HC (Fig. 3A,B), with the highest γ amplitude during the early ascending phase (corresponding to expiration and the early descending phase of local RR, Fig. 3C). We observed a similar pattern of phase-amplitude coupling during TS and Rew (Fig. 3B). However, the depth of phase-coupling was significantly reduced during TS and almost absent during Rew (Fig. 3B,C). Despite prominent RR during all three states, respiration-synchronized γ oscillations thus emerge in a behavior-dependent manner.

**Behavioral state-dependent respiration phase-coupling of prefrontal neurons**
Rhythmic breathing entrains spiking of prefrontal neurons (Biskamp et al., 2017; Zhong et al., 2017; Bagur et al., 2021; Karalis and Sirota, 2022). We thus tested whether behavioral state might affect the phase-coupling of single units to ongoing respiration (Fig. 4). To account for the pronounced asymmetry of the respiration signal, we computed instantaneous firing rates across phase bins of the OE LFP (filtered in the 1-5 Hz range), and applied a bootstrap method relying on shuffled interspike intervals to determine significant coupling (see Materials and Methods). During all three behavioral states, the majority of single units was significantly modulated by respiration, without

differences in the proportion of entrained neurons across states (Fig. 4A,B: HC: 63.8% ± 19.4, TS: 68.6% ± 13.3, Rew: 63.4% ± 20.8). During HC and Rew, units showed a significant and similar phase-preference for inspiration with a circular mean of 0.7 and 0.8 rad, respectively (Fig. 4C,D). In contrast, the cell population fired on average earlier in the respiration cycle during TS with a mean preferred phase of −1.2 rad (Fig. 4C,D). Moreover, during both TS and Rew, the neuronal population discharged more dispersed around the respiration cycle compared with HC, as reflected in a lower mean resultant population vector (vector length for HC: 0.29, TS: 0.18, Rew: 0.16, Fig. 4C,D). These results jointly suggest a behavioral state-dependent alignment of neuronal spiking with distinct phases of respiration.

Differential entrainment of pINs and pPCs by respiration
A potential explanation for the dispersed preferred phases observed on the population level during TS and Rew could be that different neuron types might show distinct and potentially nonoverlapping respiration phase preferences that result in a "blurred" tuning direction of the population as a whole. As a first distinction of unit types, we separately tested respiration entrainment of pINs and pPCs. To facilitate the identification of pINs, we performed "ground truth" control recordings in a separate cohort of mice expressing ChR-2 in PVIs ($n = 2$ mice) and extracted light-sensitive cells ($n = 9$, Fig. 5A). ChR2 expression was highly specific for PVIs in this mouse line (Fig. 5A). Lightresponsive PVIs clustered with narrow-spiking units (spike widths <0.5 ms, Fig. 5A), clearly separated from wide-spiking neurons. Based on these results, we sorted the single units recorded across behavioral states into pINs (spike width < 0.45) and pPCs (spike width > 0.53, Fig. 5B). PINs showed a significantly higher firing rate than pPCs (Fig. 5C), consistent with their fast-spiking identity. In agreement with published work
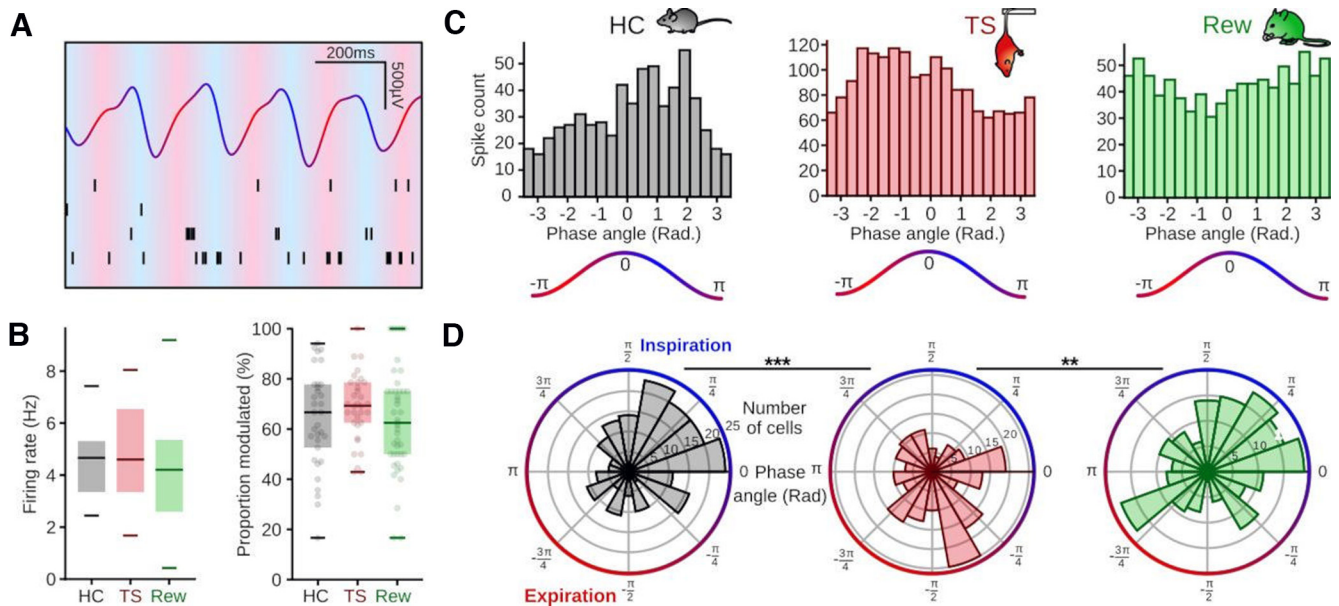
Figure 4. Behavior-dependent phase-coupling of mPFC units. **A**, Example of one second recording of the OE LFP filtered 1-12 Hz and raster plot of four cells recorded simultaneously. **B**, Left, Firing rates of prefrontal single units during HC ($n = 33$ sessions/10 mice), TS ($n = 33$ sessions/10 mice), and Rew ($n = 43$ sessions/9 mice) were not significantly different (Kruskal–Wallis test, $H = 2.61$, df $= 2$, $p = 0.27$). Right, Similar proportion of cells modulated by respiration across behaviors (Kruskal–Wallis test, $H = 1.71$, df $= 2$, $p = 0.43$). **C**, Binned spike count as a function of respiration phase of an example cell during HC (left, black) and TS (middle, red) and an example cell modulated by respiration during Rew (right, green). **D**, Preferred phases of all mPFC single units significantly modulated by respiration for the corresponding behaviors (r axis, number of cells per bin; theta axis, phase of the OE LFP in rad). Left, HC ($n = 203$ cells/10 mice, $z = 17.7$, $p = 1.5 \times 10^{-8}$). Middle, TS ($n = 215$ cells/10 mice, $z = 6.4$, $p = 0.002$). Right, Rew ($n = 197$ cells/9 mice, $z = 5.3$, $p = 0.005$, Rayleigh tests, df $= 2$). Comparisons of preferred phase: HC vs TS: df $= 416$, $p = 0.0001$, TS vs Rew: df $= 398$, $p = 0.0038$, HC vs Rew: df $= 410$, $p = 0.68$, two-sample random permutation tests. **$p < 0.01$. ***$p < 0.001$.

suggesting that interneurons might be a primary recipient of respiration-rhythmic input to the neocortex (Jung et al., 2022) and previous accounts of a large fraction of prefrontal pINs being phase-coupled to RR (Biskamp et al., 2017; Karalis and Sirota, 2022), a higher proportion of pINs compared with pPCs were modulated by respiration during HC (Fig. 5D). This was also true during Rew, with a nonsignificant trend toward this effect during TS (Fig. 5D).

PPCs and pINs displayed characteristic cell type-specific population phase preferences across behaviors (Fig. 5E): During HC, both pINs and pPCs fired at higher rate during inspiration; while during both TS and Rew, the preferred phase of pPCs scattered around the respiration cycle, with no significant preferred phase detectable on the population level (Fig. 5E, bottom). In contrast, pINs retained a preferred phase of spiking during TS but at an earlier phase of the breathing cycle (Fig. 5E). Moreover, similar to HC, pIN spiking was biased toward the inspiratory phase during Rew (Fig. 5E, top, circular mean 0.9 rad). PINs maintained a higher mean population vector length than pPCs in all conditions (HC: pIN 0.33/pPC 0.28, TS: pIN 0.48/pPC 0.09, Rew pIN 0.46/pPC 0.13), suggesting more consistent phase preference of the population of pINs compared with pPCs. On the population level, pINs thus show a specific (and behavior-dependent) preferred respiration phase, while pPCs are characterized by more heterogeneous preferred phases during TS and Rew.

Segregation of preferred respiration phase among functionally defined pPCs

Recent data identified functionally distinct prefrontal cells types with either increased or decreased activity during fear memory-related freezing. Freezing-active neurons discharged preferentially during the ascending RR phase, while neurons with reduced freezing-associated activity fired during the descending phase (Bagur et al., 2021). Based on these findings, we asked whether pPCs could be similarly grouped into functional types based on their firing response during TS or Rew, and whether such classification might reveal systematic respiration phase preferences (Fig. 6). We indeed observed cells with significant variation of their firing response at onset and offset of immobility during TS and Rew, and consequently separated pPCs into OFF cells (i.e., less active during immobility), ON cells (i.e., more active during immobility), and nonresponsive (NR) cells (Fig. 6B,E). During TS, almost half of the pPCs showed a significant change in firing rate during immobility, most of them decreasing their firing rate (i.e., OFF cells: 118 of 367, 32.2%) and a smaller proportion increasing their firing rate (i.e., ON cells: 58 of 367, 15.8%). The remaining 52% of cells showed no significant change in their firing (i.e., NR cells: 191 of 367). During Rew, we observed a comparable proportion of ON cells (59 of 384, 15.4%), with minor variation in the number of cells falling in the OFF (170 of 384, 44.3%) and NR categories (155 of 384, 40.4%). During both TS and Rew, the majority of OFF cells was significantly modulated by respiration (Fig. 6C,F, TS: 70 of 88 pPCs with sufficient activity to compute modulation analysis, 80%, Rew 122 of 165, 74%). However, similar to the total population of pPCs (Fig. 5E), the population of TS OFF cells and Rew NR cells showed no consistent preferred phase (Fig. 6C). In contrast, fewer ON cells were significantly phase-entrained by respiration (TS: 14 of 55, 34% Rew: 17 of 59, 29%), yet these populations displayed a precise preferred phase with coupling to the trough/early ascending phase, corresponding to expiration (Fig. 6C, circular mean TS: −2.9 rad, Rew: −3.0 rad). TS NR and Rew OFF cells also showed a significant bias to late expiration and beginning of expiration, respectively, but less consistent than the population of ON cells (mean population vector length: TS ON 0.75, Rew ON 0.63, TS NR 0.19, TS OFF 0.21). Neurons with enhanced activity during immobility under TS and Rew conditions thus show coupling to a specific respiration phase.
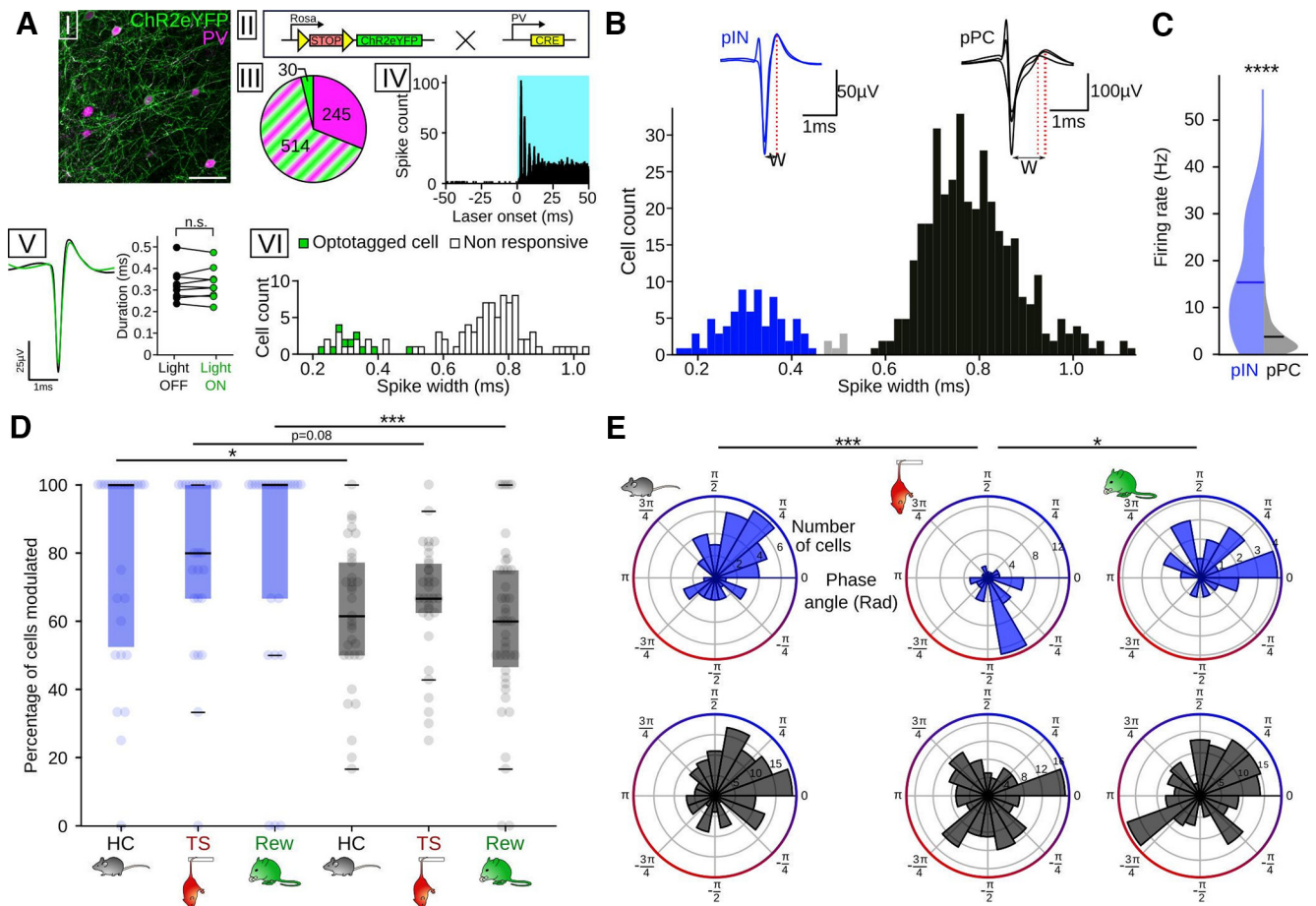
Figure 5. Differential respiration entrainment of pINs and pyramidal cells. *A*, Opto-identification of PVIs. *AI*, Immunostaining against PV (magenta) in PVxAI32 mice. Scale bar, 50 μm. *AII*, Mice for opto-identification were obtained by crossing AI32 mice (left), expressing a conditional allele of ChR2-eYPF, and a line expressing Cre-recombinase under the control of the PV promoter. The resulting offspring expresses ChR2 in PVIs. *AIII*, Cell count ($n = 3$ mice) of neurons expressing ChR2-eYFP (green), PV (magenta), or both (green and magenta stripes). *AIV*, Summed light-triggered spiking of an identified PVI centered on laser onset ($n = 1815$ stimulations, 472 nm). Note the reliable peak response occurring ~2.6 ms after laser onset. *AV*, Left, Mean spike shape of the single unit in *AIV* during baseline (black) and under light stimulation (green). Right, Spike duration did not differ between light on (green) and off conditions (black, $n = 9$ cells/2 mice, Wilcoxon signed rank test, T = 21, df = 8, $p = 0.91$). *AVI*, Binned spike widths of opto-identified PVIs (green) and nonresponsive cells recorded simultaneously (white). All identified PVIs had a spike width < 0.5 ms. *B*, Top, Example of the spike shape of a pIN (blue) and pPC (black). W, Spike width. Bottom, Binned spike widths of prefrontal neurons recorded in HC. Blue represents pINs ($n = 76$). Black represents pPCs ($n = 367$). Gray represents unclassified cells ($n = 6$). Three outliers (spike width 1.61, 1.63, and 2.64 ms) are omitted from the histogram. *C*, Firing rate of pINs (blue, $n = 76$) and pPCs (black, $n = 367$) during HC. PINs had a significantly higher firing rate ($t = 15.15$, df = 441, $p = 4.7 \times 10^{-42}$, unpaired t test). *D*, Percentage of cells modulated by respiration (pIN HC: $n = 26$ sessions/10 mice; pIN TS: $n = 26$ sessions/10 mice; pIN Rew: $n = 25$ sessions/8 mice; pPC HC: $n = 33$ sessions/10 mice; pPC TS: $n = 33$ sessions/10 mice; pPC Rew: $n = 42$ sessions/9 mice). Two-way ANOVA for an effect of cell type: $F = 17.87$, df = 1, $p = 0.0004$, HC: $z = 2.59$, $p = 0.029$; TS: $z = 2.18$, $p = 0.08$; Rew: $z = 3.63$, $p = 0.008$, Dunn *post hoc* tests, df = 5). *E*, Same as in Figure 4D, but segregated for pIN (top, blue, HC: $n = 48$ cells; TS: $n = 46$ cells; Rew: $n = 22$ cells) and pPC (bottom, black, HC: $n = 165$ cells; TS: $n = 154$ cells; Rew: $n = 172$ cells). All measures of preferred population phase, except for pPC during TS ($z = 1.2$, $p = 0.297$) and pPC during Rew ($z = 2.7$, $p = 0.067$), showed a significant nonuniform distribution ($z = 12.7$-5.3, $p = 2.4 \times 10^{-6}$ to $p = 0.004$, Rayleigh tests, df = 2). Preferred phases: PIN: HC vs TS: df = 50, $p = 8 \times 10^{-5}$; Rew vs TS: df = 50, $p = 0.004$; all other comparisons, $p > 0.82$, two-sample random permutation tests with Bonferroni correction. *$p < 0.05$. ***$p < 0.001$. ****$p < 0.0001$.

Layer and behavioral state-specific modulation of mPFC pPCs

Previous work identified respiration-rhythmic current sinks in deep layers of the mPFC (layer V/VI), suggesting that synaptic drive transmitting breathing-synchronous input to the mPFC targets predominantly deep layers (Karalis and Sirota, 2022). These results prompted us to test whether neurons situated in deep (layer V/VI) versus superficial layers (layer II/III) might be differently entrained by respiration in a behavior-dependent manner. Thus, we separated pPCs depending on their laminar location in either superficial ($n = 267$, 107 during HC and TS and 160 during Rew) or deep mPFC layers ($n = 424$, 211 during HC and TS and 213 during Rew, Fig. 7A). There was no difference in the preferred phase of respiration-coupling for the population of pPC in superficial and deep layers (Fig. 7B, HC: df = 43, $p = 0.93$, TS: df = 39, $p = 0.59$, Rew: df = 167, $p = 0.26$, two sample random

permutation tests). We furthermore did not observe major changes in pPC firing rates across layers and behavioral states, except for a relative decrease in the firing rate of superficial layer pPCs compared with deep layer pPCs during Rew (Fig. 7C). Consistent with the presence of respiration-rhythmic current sinks in deep prefrontal layers (Karalis and Sirota, 2022), we found a higher proportion of cells modulated in the deep layers during HC (Fig. 7D). Similarly, Rew was characterized by a large proportion of respiration-coupled neurons in deep layers with a trend toward a lower proportion of coupled neurons in the superficial layers (Fig. 7D). In contrast, during TS, the proportion of phase-coupled neurons in superficial layers was significantly increased compared with both HC and Rew (Fig. 7D). These results suggest a dynamic layer- and behavior-dependent recruitment of mPFC neurons by respiration-rhythmic inputs.
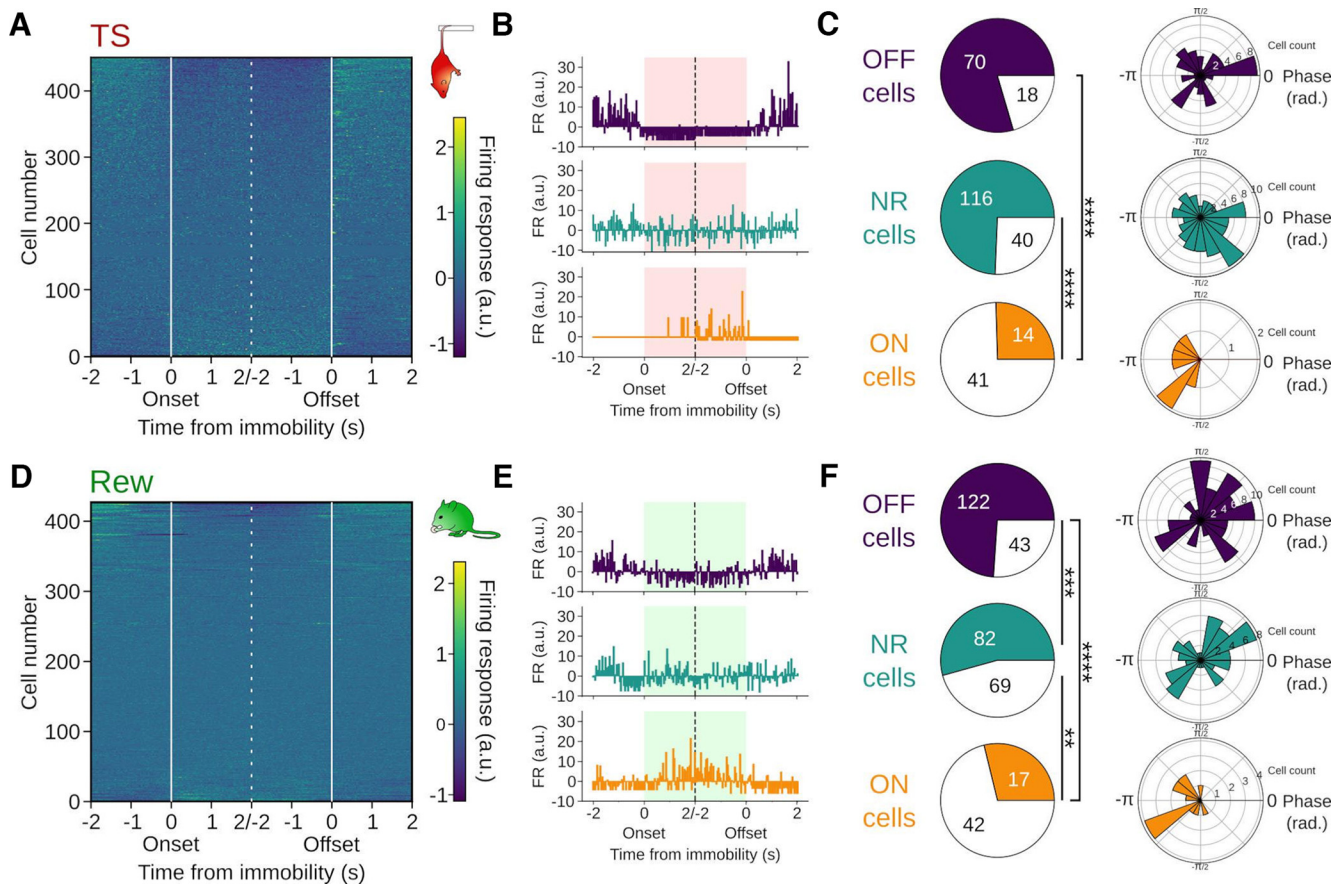
Figure 6. Respiration entrainment of functionally distinct types of pPCs. **A**, **D**, Mean firing rate (z-scored) of all mPFC single units aligned to immobility onset and offset during TS (**A**, n = 449 cells/10 mice) and Rew (**D**, n = 428 cells/9 mice). Cells are shown sorted by their activity during immobility. **B**, **E**, Summed firing responses of pPCs aligned to immobility onset and offset. Firing response was computed as the z score of 4 s binned spike train snippets centered on behavioral transitions. Top, Example of an OFF cell: pPC with a significant change in firing response at transition and a decrease in firing rate during immobility. Middle, Example cell with no firing response (NR). Bottom, Example of an ON cell: pPC with a significant change in firing response at transition and an increase in firing rate during immobility. **C**, **F**, Left, Proportion of pPCs modulated by respiration among the OFF (**C**, n = 88 cells/7 mice; **F**, n = 165 cells/9 mice), NR (**C**, n = 156 cells/8 mice; **F**, n = 151 cells/9 mice), and ON cells (**C**, n = 55 cells/9 mice; **F**, n = 59 cells/8 mice). TS: OFF vs ON: p = 0, ON vs NR: p = 0, OFF vs NR: p = 0.097, χ^2 = 60.34, df = 2. Rew: OFF vs ON: p = 0, ON vs NR: p = 0.0009, OFF vs NR: p = 0.0003, χ^2 = 38.81, df = 2. Right, Preferred respiration phase of pPCs for significantly respiration-entrained OFF, NR, and ON cells. Both ON populations (TS: z = 3.9, p = 0.014, Rew: z = 5.1, p = 0.004), Rew OFF (z = 4.3, p = 0.014), and TS NR cells (z = 3.1, p = 0.04) but not TS OFF (z = 0.4, p = 0.695) and Rew NR cells (z = 1.1, p = 0.348, Rayleigh tests, df = 2) showed a significant nonuniform distribution. Significance thresholds after Bonferroni correction: **p < 0.003; ***p < 0.0003; ****p < 0.00,003.

Discussion

We evaluated respiration entrainment of prefrontal activity during distinct immobile states of HC, TS, and Rew (Fig. 8). First, the breathing rhythm itself changed in regularity and frequency. Second, while RR was apparent across all states, the phase-amplitude coupling between respiration and prefrontal γ was attenuated during TS and Rew compared with HC. Third, entrainment of prefrontal single units by respiration was state-dependent: PINs displayed clear preferred phases as a population in all states, but shifted from inspiration to fire at an earlier phase of the breathing rhythm during TS. While we confirmed that during HC most prefrontal pPC fired during inspiration, we saw a redistribution of the pPC activity along the respiration cycle during TS and Rew, with immobility-active neurons showing a highly consistent respiration phase. Finally, during TS, we observed a specific increase in the proportion of cells modulated by respiration in the superficial layers.

Compared with the other states under investigation in this study, the breathing rhythm was more regular and slower during TS. This breathing rhythm was similar to the one observed during freezing in rodents (Moberly et al., 2018; Bagur et al., 2021;

Karalis and Sirota, 2022), suggesting that regular ~4 Hz breathing might represent a common respiratory pattern under stress/anxiety. The slow and deep breathing rhythm during TS generated the strongest RR compared with HC and Rew consumption. During freezing, the 4 Hz rhythm plays a role in synchronizing the PFC and the amygdala (Dejean et al., 2016; Karalis et al., 2016), and has been recently shown to be instrumental in controlling the maintenance of freezing epochs (Moberly et al., 2018; Bagur et al., 2021). It remains to be investigated whether the steady RR during TS immobility might play a similar role in controlling the duration of immobile epochs in this paradigm.

γ oscillations show phase-amplitude coupling with prefrontal RR across species (Kluger and Gross, 2021; González et al., 2023). Prefrontal γ bursts are thought to be generated in a reafferent mechanism by polysynaptic transmission from the OB, via olfactory cortex, to the mPFC (Karalis and Sirota, 2022). Since ~10% of prefrontal pyramidal neurons are phase-modulated by local γ oscillations, respiration-entrained γ bursts might reflect the local processing of sensory input impinging from the olfactory system (Karalis and Sirota, 2022). Interestingly, entrainment of γ bursts was stronger during HC than during either TS or Rew. This suggests that the temporal coordination of the local
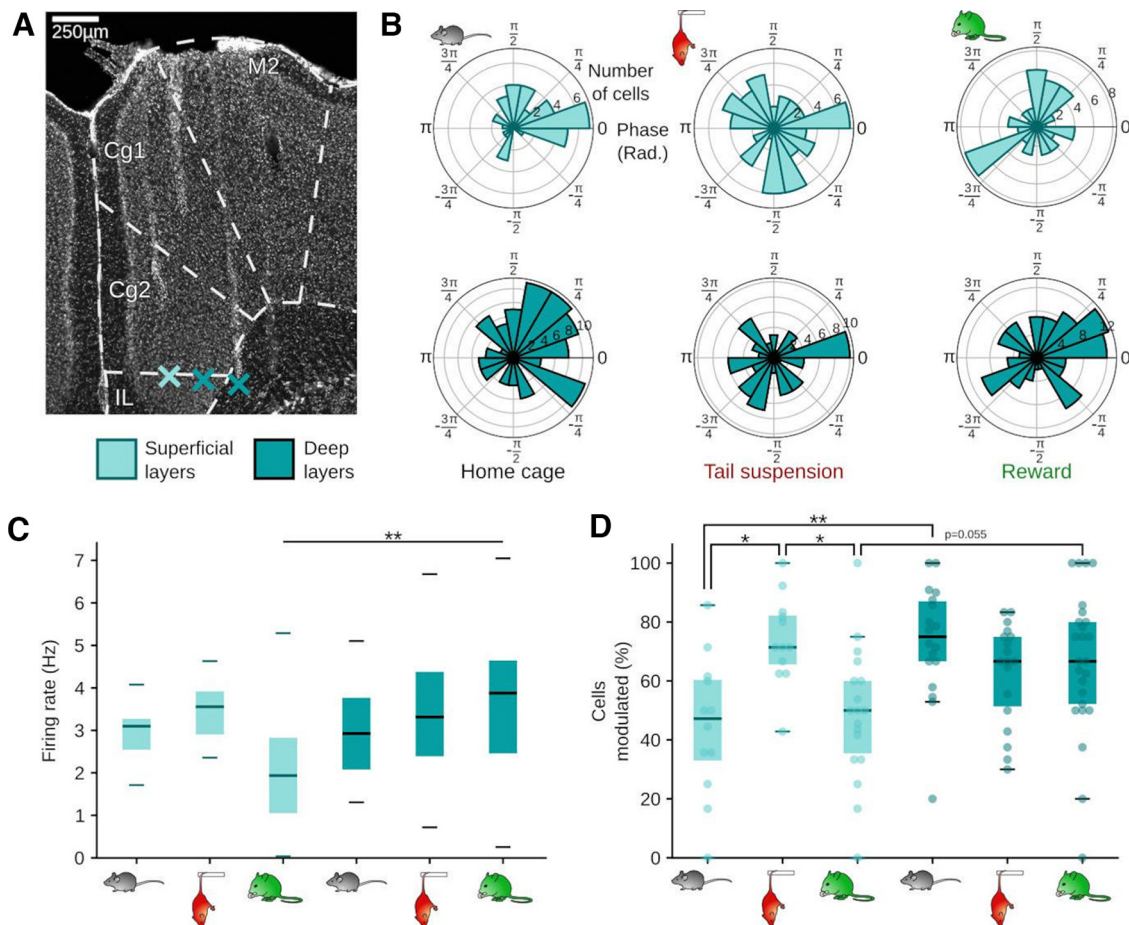
Figure 7. Layer- and behavior-specific modulation of prefrontal cells by respiration. ***A***, Prefrontal coronal section stained with DAPI. Asterisks indicate the tips of the shanks of a silicon probe in superficial (layers II/III) and deep layers (V/VI). ***B***, Preferred phase of respiration-entrained pPCs in superficial (light blue, top) and deep layers (dark blue, bottom). R axis, number of cells per bin; theta axis, respiration phase in rads. ***C***, Mean firing rate of pPCs in superficial (left, light blue, HC & TS $n = 12$ sessions/4 mice, Rew $n = 18$ sessions/5 mice) and deep layers (right, dark blue, HC & TS $n = 18$ sessions/6 mice, Rew $n = 25$ sessions/6 mice). Two-way ANOVA (layer: $F = 5.02$, df = 1, $p = 0.027$, behavioral state: $F = 1.05$, df = 2, $p = 0.353$, interaction layer × behavioral state: $F = 4.27$, df = 2, $p = 0.017$; Rew superficial vs deep: $z = 3.57$, $p = 0.003$, all other comparisons $p > 0.06$, post hoc Dunn tests, df = 5). ***D***, Percentage of respiration-modulated pPCs in superficial (left, light blue, HC & TS $n = 12$ sessions/4 mice, Rew $n = 18$ sessions/5 mice) and deep layers (right, dark blue, HC & TS $n = 18$ sessions/6 mice, Rew $n = 25$ sessions/6 mice, two-way ANOVA: layer: $F = 8.99$, df = 1, $p = 0.003$, behavioral state: $F = 1.30$, df = 2, $p = 0.28$, interaction layer × behavioral state: $F = 6.92$, df = 2, $p = 0.002$; superficial vs deep: HC: $z = 3.37$, $p = 0.007$, TS: $z = 1.35$, $p = 1$, Rew: $z = 3.57$, $p = 0.003$, superficial layers: HC vs TS: $z = 3.02$, $p = 0.02$, TS vs Rew: $z = 3.08$, $p = 0.02$, all other comparisons $p > 0.05$, post hoc Dunn tests, df = 5). *$p < 0.05$. **$p < 0.01$.

processing of sensory input in form of respiration-synchronous γ bursts might represent a default state of the mPFC network most strongly observable under baseline conditions (i.e., HC). The mechanisms of behavioral state-dependent changes in γ modulation depth are likely complex. In a reduced graph theory model, slow oscillatory input is sufficient to generate γ oscillation-like activity fluctuations (Heck et al., 2017). The model suggests a correlation between the strength of the rhythmic input signal and the depth of phase-amplitude coupling of γ oscillations (Heck et al., 2017). TS was associated with a stronger impact of respiration-rhythmic drive but lower γ phase-amplitude coupling compared with HC (Figs. 2 and 3), suggesting that additional factors besides the amplitude of breathing-synchronized input modulates γ coupling. Optogenetic silencing experiments and spike-triggered γ amplitude analyses suggest PVIs as drivers of prefrontal γ oscillations (Sohal et al., 2009; Sauer and Bartos, 2022). While the majority of PVIs coupled to the descending respiration phase in HC, some PVIs preferred the early ascending phase (in which γ oscillations are nested, Fig. 3). Our data suggest that fewer PVIs might phase-couple to this "γ phase" or respiration during TS and Rew (Fig. 7E). However,

larger samples of identified PVIs would be required to draw quantitative conclusions. An additional possibility is that neuromodulators impact γ coupling depending on the behavioral state: TS exposure increases dopamine concentration in the mPFC (Kolata et al., 2018). *In vivo* uncaging experiments suggested that dopamine enhances phase-amplitude coupling between δ and γ oscillations in awake rats (Andino-Pavlovsky et al., 2017). While the direction of the change in δ-γ coupling does not match our observations of reduced respiration-γ coupling during TS, it remains to be tested whether dopamine or other neuromodulators released in the mPFC during TS or Rew might affect respiration-γ coupling.

Our analysis of respiration phase-coupling across HC, TS, and Rew extends on previous observations comparing defined behavioral states. Parietal cortex neurons display distinct preferred respiration phases during REM, NREM, and wake immobile epochs (Jung et al., 2023). Interestingly, during awake immobility (comparable to our HC condition), parietal cortex neurons fire during expiration while our phase-coupling analysis revealed that prefrontal pPCs fire preferentially linked to inspiration (Jung et al., 2023). Inspiration-linked firing of mPFC
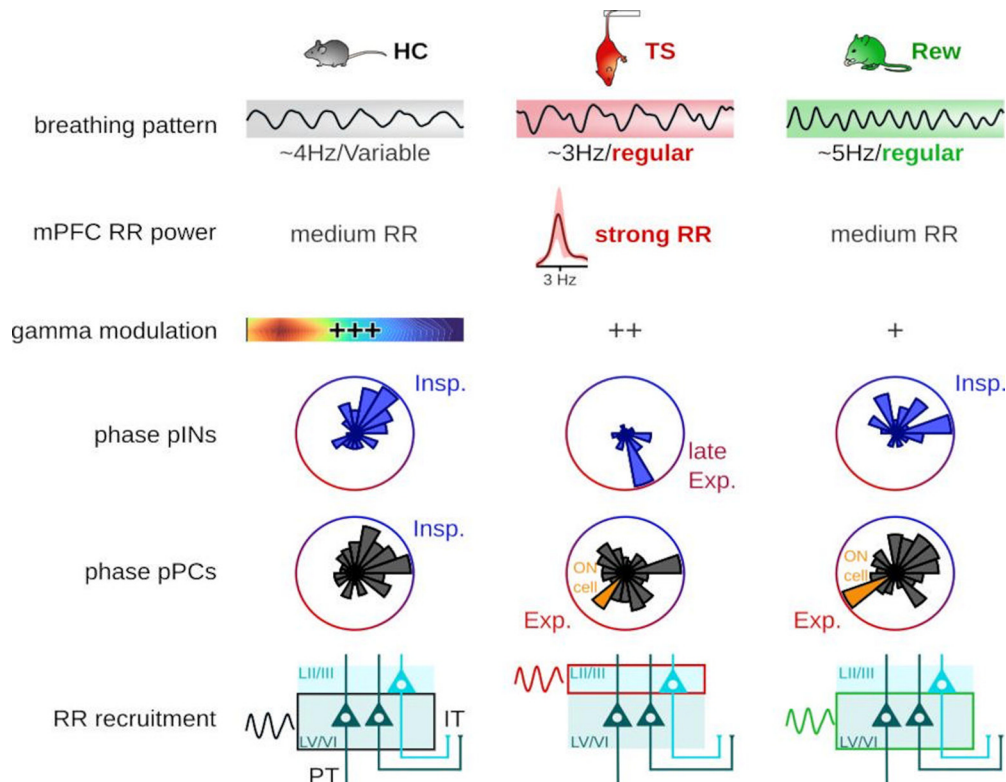
Figure 8. Summary of respiration entrainment of mPFC neuronal activity across behavioral states. Top to bottom, The breathing pattern was characteristic of each behavioral state in frequency and regularity, with regular breathing emerging during TS and Rew. Significant modulation (see Fig. 3) of 85 Hz prefrontal γ oscillations by respiration occurred in all states, but the phase-amplitude coupling was strongest during HC (+++). Firing of pINs showed a preferred and behavior-specific respiration phase as a population. During immobility linked with strong emotions, the prefrontal pPC population scattered along the respiration cycle. Functionally relevant ON cells, which increased their firing during immobility, phase-coupled to expiration (Exp.). During HC and Rew, the highest proportion of pPCs modulated by the respiration were located in deep layers (LV/VI) of the PFC, where both pyramidal tract (PT) and IT neurons are found. During TS, the proportion of cells modulated in the superficial layers (LII/III), where IT cells are found, increased.

neurons is consistent with previous accounts (Karalis and Sirota, 2022). These results thus suggest area-specific preferred phases during awake immobility. During TS and Rew, preferred phases redistributed along the respiration cycle. That observation bears similarity to respiration coupling during freezing after fear conditioning, when the population of pPCs tiles the entire respiration cycle (Bagur et al., 2021). However, functionally defined neurons display specific RR coupling during freezing, namely, with freezing-active neurons coupling to the ascending phase and "freezing-off" neurons to the descending phase of RR (Bagur et al., 2021). Extending on that observation, we found that immobility-active neurons during both TS and Rew fired preferably during the trough/early ascending phase of respiration (expiration). This functionally defined population of cells thus discharged maximally ∼180° opposite of the preferred phase of the pPC population during HC. Notably, the preferred phase of the immobility-active population identified here differs from that of freezing-active neurons, which activate during the descending respiration phase. These results thus suggest specific respiration-coupling regimens depending on the "type" of immobility.

It was previously noted that the recruitment of prefrontal neurons by respiration and local RR depends on their laminar location (Karalis and Sirota, 2022). Specifically, deep layer neurons are more frequently entrained than superficial cells. The specific increase in superficial layer respiration coupling during TS as identified in this study suggests additional complexity of respiration entrainment such that neurons of different laminar position can be recruited to the respiration rhythm in a

behavior-dependent manner. The mechanisms of the recruitment of superficial layer neurons to respiration drive remain elusive. Deep layers are composed of both intratelencephalic (IT) neurons with projections within the neocortex and to the striatum, and pyramidal tract neurons that project outside of the telencephalon (Oberlaender et al., 2012; Harris and Shepherd, 2015). In contrast, superficial layers contain largely IT neurons (Harris and Shepherd, 2015). It is thus likely that the enhanced entrainment of superficial layers reflects the respiration-synchronized spiking of IT neurons. Groups of IT neurons of distinct regions of the neocortex that fire during the same respiration phase might represent a mechanism to facilitate the synchronization of cell assemblies spanning across communicating neocortical areas. This hypothesis could be tested in the future by systematic investigations of layer- and cell type-specific measurements of respiration coupling across neocortical areas.

The behavioral states investigated in this study are set apart from each other in several ways: First, they likely differ in terms of the emotional valence associated with them. Extended TS immobility has traditionally been interpreted as depression-related behavior, which has been criticized for the lack of face and construct validity (Commons et al., 2017). Rather, TS models a behavioral response to an acutely stressful intervention ("behavioral challenge") (Warden et al., 2012; Commons et al., 2017). Prefrontal dopamine release, as observed during TS (Kolata et al., 2018), is robustly linked with aversive experiences: tail shock, a classic aversive stimulus, increases prefrontal dopamine concentration, presumably by dopamine release from VTA-mPFC projections (Abercrombie et al., 1989; Kim et

al., 2016). Moreover, plantar injection of formalin to generate irritation results in an enhanced AMPAR/NMDAR ratio in mPFC-projecting dopaminergic VTA neurons, suggestive of synaptic potentiation at inputs driving these neurons (Kauer and Malenka, 2007; Lammel et al., 2011). Reward consumption is likely perceived as positive: Delivery of water rewards induces dopamine release from VTA terminals in the NAC (Kim et al., 2016). Accumbens-projecting VTA cells are thought to mediate rewarding experience, as suggested by synaptic potentiation of inputs to these neurons by cocaine (Lammel et al., 2011). Second, body posture differed between the behaviors, in particular during TS, and Rew required food restriction for motivation. It can thus not be excluded that differing vestibular signals or satiety levels might have affected some of the metrics studied here. Finally, we showed significant variations of the respiration pattern itself across behaviors, such as peak frequency and regularity, which might account in part for the distinct entrainment of prefrontal neuronal activity.

In conclusion, our results add to the notion of internal feedback mechanisms by which intrinsic rhythms of the body modulate cognition (Tort et al., 2018a; Azzalini et al., 2019; Heck et al., 2019) and suggest that respiration exerts complex influences on neuronal activity in the mPFC by pacing local discharges in a behavior-, cell type-, and layer-specific manner.

References

Abercrombie ED, Keefe KA, DiFrischia DS, Zigmond MJ (1989) Differential effect of stress on in vivo dopamine release in striatum, nucleus accumbens, and medial frontal cortex. J Neurochem 52:1655–1658.

Adrian ED (1942) Olfactory reactions in the brain of the hedgehog. J Physiol 100:459–473.

Amarante LM, Caetano MS, Laubach M (2017) Medial frontal theta is entrained to rewarded actions. J Neurosci 37:10757–10769.

Amarante LM, Laubach M (2021) Coherent theta activity in the medial and orbital frontal cortices encodes reward value. Elife 10:e63372.

Andino-Pavlovsky V, Souza AC, Scheffer-Teixeira R, Tort AB, Etchenique R, Ribeiro S (2017) Dopamine modulates delta-gamma phase-amplitude coupling in the prefrontal cortex of behaving rats. Front Neural Circuits 11:29.

Arshamian A, Iravani B, Majid A, Lundström JN (2018) Respiration modulates olfactory memory consolidation in humans. J Neurosci 38:10286–10294.

Azzalini D, Rebollo I, Tallon-Baudry C (2019) Visceral signals shape brain dynamics and cognition. Trends Cogn Sci 23:488–509.

Bagur S, Lefort JM, Lacroix MM, de Lavilléon G, Herry C, Chouvaeff M, Billand C, Geoffroy H, Benchenane K (2021) Breathing-driven prefrontal oscillations regulate maintenance of conditioned-fear evoked freezing independently of initiation. Nat Commun 12:2605.

Biskamp J, Bartos M, Sauer JF (2017) Organization of prefrontal network activity by respiration-related oscillations. Sci Rep 7:45508.

Carney RS (2019) Ultrasonic vocalizations emitted during defensive behavior alter the influence of the respiratory rhythm on brain oscillatory dynamics in the fear circuit of rats. eNeuro 6:ENEURO.0280-19.2019.

Chung JE, Magland JF, Barnett AH, Tolosa VM, Tooker AC, Lee KY, Shah KG, Felix SH, Frank LM, Greengard LF (2017) A fully automated approach to spike sorting. Neuron 95:1381–1394.e6.

Commons KG, Cholanians AB, Babb JA, Ehlinger DG (2017) The rodent forced swim test measures stress-coping strategy, not depression-like behavior. ACS Chem Neurosci 8:955–960.

Connelly T, Yu Y, Grosmaitre X, Wang J, Santarelli LC, Savigner A, Qiao X, Wang Z, Storm DR, Ma M, Carlson JR (2015) G protein-coupled odorant receptors underlie mechanosensitivity in mammalian olfactory sensory neurons. Proc Natl Acad Sci USA 112:590–595.

Courtiol E, Amat C, Thévenet M, Messaoudi B, Garcia S, Buonviso N (2011) Reshaping of bulbar odor response by nasal flow rate in the rat. PLoS One 6:e16445.

Dejean C, Courtin J, Karalis N, Chaudun F, Wurtz H, Bienvenu TC, Herry C (2016) Prefrontal neuronal assemblies temporally control fear behaviour. Nature 535:420–424.

Folschweiller S, Sauer J (2022) Phase-specific pooling of sparse assembly activity by respiration-related brain oscillations. J Physiol 600:1991–2011.

Franklin KBJ, Paxinos G (2007) The mouse brain in stereotaxic coordinates, 3rd Ed. Elesevier.

Girin B, Juventin M, Garcia S, Lefèvre L, Amat C, Fourcaud-Trocmé N, Buonviso N (2021) The deep and slow breathing characterizing rest favors brain respiratory-drive. Sci Rep 11:7044.

González J, Cavelli M, Mondino A, Castro-Zaballa S, Brankačk J, Draguhn A, Torterolo P, Tort AB (2023) Breathing modulates gamma synchronization across species. Pflugers Arch 475:49–63.

Grosmaitre X, Santarelli LC, Tan J, Luo M, Ma M (2007) Dual functions of mammalian olfactory sensory neurons as odor detectors and mechanical sensors. Nat Neurosci 10:348–354.

Grund M, Al E, Pabst M, Dabbagh A, Stephani T, Nierhaus T, Gaebler M, Villringer A (2022) Respiration, heartbeat, and conscious tactile perception. J Neurosci 42:643–656.

Harris KD, Shepherd GM (2015) The neocortical circuit: themes and variations. Nat Neurosci 18:170–181.

Heck DH, McAfee SS, Liu Y, Babajani-Feremi A, Rezaie R, Freeman WJ, Wheless JW, Papanicolaou AC, Ruszinkó M, Sokolov Y, Kozma R (2017) Breathing as a fundamental rhythm of brain function. Front Neural Circuits 10:115.

Heck DH, Kozma R, Kay LM (2019) The rhythm of memory: how breathing shapes memory function. J Neurophysiol 122:563–571.

Horst N, Laubach M (2013) Reward-related activity in the medial prefrontal cortex is driven by consumption. Front Neurosci 7:56.

Ito J, Roy S, Liu Y, Cao Y, Fletcher M, Lu L, Boughter JD, Grün S, Heck DH (2014) Whisker barrel cortex delta oscillations and gamma power in the awake mouse are linked to respiration. Nat Commun 5:10.

Johannknecht M, Kayser C (2022) The influence of the respiratory cycle on reaction times in sensory-cognitive paradigms. Sci Rep 12:2586.

Jung F, Witte V, Yanovsky Y, Klumpp M, Brankačk J, Tort AB, Draguhn A (2022) Differential modulation of parietal cortex activity by respiration and θ oscillations. J Neurophysiol 127:801–817.

Jung F, Yanovsky Y, Brankačk J, Tort AB, Draguhn A (2023) Respiratory entrainment of units in the mouse parietal cortex depends on vigilance state. Pflugers Arch 475:65–76.

Karalis N, Sirota A (2022) Breathing coordinates cortico-hippocampal dynamics in mice during offline states. Nat Commun 13:1–20.

Karalis N, Dejean C, Chaudun F, Khoder S, Rozeske R, Wurtz H, Bagur S, Benchenane K, Sirota A, Courtin J, Herry C (2016) 4-Hz oscillations synchronize prefrontal-amygdala circuits during fear behavior. Nat Neurosci 19:605–612.

Kauer JA, Malenka RC (2007) Synaptic plasticity and addiction. Nat Rev Neurosci 8:844–858.

Kim CK, Yang SJ, Pichamoorthy N, Young NP, Kauvar I, Jennings JH, Lerner TN, Berndt A, Lee SY, Ramakrishnan C, Davidson TJ, Inoue M, Bito H, Deisseroth K (2016) Simultaneous fast measurement of circuit dynamics at multiple sites across the mammalian brain. Nat Methods 13:325–328.

Kluger DS, Gross J (2021) Respiration modulates oscillatory neural network activity at rest. PLoS Biol 19:e3001457.

Kluger DS, Balestrieri E, Busch NA, Gross J (2021) Respiration aligns perception with neural excitability. Elife 10:e70907.

Kolata SM, Nakao K, Jeevakumar V, Farmer-Alroth EL, Fujita Y, Bartley AF, Jiang SZ, Rompala GR, Sorge RE, Jimenez DV, Martinowich K, Mateo Y, Hashimoto K, Dobrunz LE, Nakazawa K (2018) Neuropsychiatric phenotypes produced by GABA reduction in mouse cortex and hippocampus. Neuropsychopharmacology 43:1445–1456.

Lammel S, Ion DI, Roeper J, Malenka RC (2011) Projection-specific modulation of dopamine neuron synapses by aversive and rewarding stimuli. Neuron 70:855–862.

Lane G, Zhou G, Noto T, Zelano C (2020) Assessment of direct knowledge of the human olfactory system. Exp Neurol 329:113304.

Liu Y, McAfee SS, Heck DH (2017) Hippocampal sharp-wave ripples in awake mice are entrained by respiration. Sci Rep 7:8950.

Lockmann AL, Laplagne DA, Leão RN, Tort AB (2016) A respiration-coupled rhythm in the rat hippocampus independent of theta and slow oscillations. J Neurosci 36:5338–5352.

Moberly AH, Schreck M, Bhattarai JP, Zweifel LS, Luo W, Ma M (2018) Olfactory inputs modulate respiration-related rhythmic activity in the prefrontal cortex and freezing behavior. Nat Commun 9:1528.

Mofleh R, Kocsis B (2021) Respiratory coupling between prefrontal cortex and hippocampus of rats anaesthetized with urethane in theta and non-theta states. Eur J Neurosci 54:5507–5517.

Nakamura NH, Fukunaga M, Oku Y (2018) Respiratory modulation of cognitive performance during the retrieval process. PLoS One 13:e0204021.

Nguyen Chi V, Müller C, Wolfenstetter T, Yanovsky Y, Draguhn A, Tort AB, Brankačk J (2016) Hippocampal respiration-driven rhythm distinct from theta oscillations in awake mice. J Neurosci 36:162–177.

Noto T, Zhou G, Schuele S, Templer J, Zelano C (2018) Automated analysis of breathing waveforms using BreathMetrics: a respiratory signal processing toolbox. Chem Senses 43:583–597.

Oberlaender M, de Kock CP, Bruno RM, Ramirez A, Meyer HS, Dercksen VJ, Helmstaedter M, Sakmann B (2012) Cell type-specific three-dimensional structure of thalamocortical circuits in a column of rat vibrissal cortex. Cereb Cortex 22:2375–2391.

Rojas-Líbano D, Wimmer del Solar J, Aguilar-Rivera M, Montefusco-Siegmund R, Maldonado PE (2018) Local cortical activity of distant brain areas can phase-lock to the olfactory bulb's respiratory rhythm in the freely behaving rat. J Neurophysiol 120:960–972.

Sauer JF, Bartos M (2022) Disrupted-in-schizophrenia-1 is required for normal pyramidal cell–interneuron communication and assembly dynamics in the prefrontal cortex. Elife 11:e79471.

Sauer JF, Strüber M, Bartos M (2015) Impaired fast-spiking interneuron function in a genetic mouse model of depression. Elife 4:e04979.

Sohal VS, Zhang F, Yizhar O, Deisseroth K (2009) Parvalbumin neurons and gamma rhythms enhance cortical circuit performance. Nature 459:698–702.

Tort AB, Brankačk J, Draguhn A (2018a) Respiration-entrained brain rhythms are global but often overlooked. Trends Neurosci 41:186–197.

Tort AB, Ponsel S, Jessberger J, Yanovsky Y, Brankačk J, Draguhn A (2018b) Parallel detection of theta and respiration-coupled oscillations throughout the mouse brain. Sci Rep 8:6432.

Wachowiak M (2011) All in a sniff: olfaction as a model for active sensing. Neuron 71:962–973.

Warden MR, Selimbeyoglu A, Mirzabekov JJ, Lo M, Thompson KR, Kim SY, Adhikari A, Tye KM, Frank LM, Deisseroth K (2012) A prefrontal cortex-brainstem neuronal projection that controls response to behavioural challenge. Nature 492:428–432.

Yanovsky Y, Ciatipis M, Draguhn A, Tort AB, Brankačk J (2014) Slow oscillations in the mouse hippocampus entrained by nasal respiration. J Neurosci 34:5949–5964.

Zelano C, Jiang H, Zhou G, Arora N, Schuele S, Rosenow J, Gottfried JA (2016) Nasal respiration entrains human limbic oscillations and modulates cognitive function. J Neurosci 36:12448–12467.

Zhong W, Ciatipis M, Wolfenstetter T, Jessberger J, Müller C, Ponsel S, Yanovsky Y, Brankačk J, Tort AB, Draguhn A (2017) Selective entrainment of gamma subbands by different slow network oscillations. Proc Natl Acad Sci USA 114:4519–4524.